BNL-229088-2025-JAAM

Atomically Revealing Bulk Point Defect Dynamics in HydrogenDriven γ Fe2O3 → Fe3O4 → FeO Transformation

Y. Wu, M. R. Li

To be published in "Advanced Functional Materials"

October 2025

Center for Functional Nanomaterials

Brookhaven National Laboratory

U.S. Department of Energy

USDOE Office of Science (SC), Basic Energy Sciences (BES). Scientific User Facilities (SUF)

DISCLAIMER

ADVANCED FUNCTIONAL MATERIALS
www.afm-journal.de

Atomically Revealing Bulk Point Defect Dynamics in Hydrogen-Driven γ-Fe_2O_3 → Fe_3O_4 → FeO Transformation

*Yupeng Wu, Dongxiang Wu, Wenhui Zhu, Xiaobo Chen, Zhikang Zhou, Zhilu Liang, Shuonan Ye, Meng Li, Xiao Tong, Kim Kisslinger, Sooyeon Hwang, Dmitri Zakharov, Renu Sharma, Judith C. Yang, and Guangwen Zhou**

Understanding how point defects in the bulk govern redox transformations is essential for advancing hydrogen-based metal production and designing high-performance oxide materials. This study reveals the atomic-scale mechanisms driving hydrogen-induced reduction of γ-Fe_2O_3 to Fe_3O_4, focusing on how bulk vacancy dynamics dictate structural evolution and reaction kinetics. A key finding is the pronounced contrast in defect behavior between the two oxides: in γ-Fe_2O_3, intrinsic Fe vacancies promote oxygen vacancy clustering, destabilizing the local lattice and driving nanopore formation. In contrast, Fe_3O_4 exhibits a higher oxygen vacancy formation energy and lacks intrinsic Fe vacancies, suppressing vacancy aggregation and maintaining a dense, pore-free structure. This divergence governs distinct reduction pathways—γ-Fe_2O_3 undergoes an interface-reaction-limited transformation confined to the γ-Fe_2O_3/Fe_3O_4 boundary, while Fe_3O_4 supports a uniform increase in oxygen vacancy concentration, enabling bulk-phase reduction to lower-oxide FeO. Integrated in situ electron microscopy and density functional theory modeling uncover a vacancy-mediated mechanism, where synergistic cation-anion vacancy dynamics steer microstructure evolution and phase progression. These insights highlight the critical role of vacancy dynamics in controlling oxide reactivity and offer a pathway toward vacancy engineering to enhance reduction kinetics in hydrogen metallurgy and to tailor porosity, reactivity, and structural resilience in oxide-based catalysts and energy materials.

1. Introduction

The smelting of metallic iron has been pivotal in human civilization,[1–4] yet conventional blast-furnace ironmaking remains carbon-intensive, contributing ≈7–9% of global CO_2 emissions.[5–8] Hydrogen-based reduction of iron oxides offers a transformative, low-carbon alternative by replacing CO_2 emissions with water vapor as the byproduct of the reduction reaction.[9–13] However, this process is inherently complex due to the multiple oxidation states of Fe, which give rise to a sequence of intermediate phases, including hematite (α-Fe_2O_3), maghemite (γ-Fe_2O_3), magnetite (Fe_3O_4), and wüstite (FeO),[14] each exhibiting distinct thermodynamic stabilities and kinetic behaviors. Bulk measurements such as temperature-programmed reduction (TPR)[15] and X-ray diffraction (XRD)[14,16,17] have established two principal reduction pathways: (i) Fe_2O_3 → Fe_3O_4 → FeO → Fe, and (ii) Fe_2O_3 → Fe_3O_4 → Fe (bypassing FeO). The choice of a given pathway is influenced by temperature, gas composition and pressure, crystallography, and—critically—defect chemistry.[18,19]

While previous in situ environmental transmission electron microscopy (TEM) studies have provided atomic-scale insights into the stepwise reduction of α-Fe_2O_3 to metallic Fe,[20–24] key mechanistic questions remain unresolved. In particular, under H_2, α-Fe_2O_3 often undergoes a transient transformation into γ-Fe_2O_3 through progressive lattice oxygen (O) removal.[20,21,25] This intermediate spinel structure contains a high concentration of intrinsic Fe vacancies, which may play a critical role in driving defect formation and structural evolution. In contrast, Fe_3O_4 lacks such intrinsic Fe vacancies and higher O vacancy (V_O) formation energies—suggesting fundamentally different reduction behavior compared to γ-Fe_2O_3. However, the interplay between vacancy dynamics, phase transitions, and microstructural evolution in γ-Fe_2O_3 and Fe_3O_4 remains unexplored.

Here, we employ environmental TEM[26–31] to directly visualize the H_2-driven reduction of γ-Fe_2O_3 and Fe_3O_4 with atomic-scale resolution. Our observations reveal a striking contrast in defect behavior between the two phases: γ-Fe_2O_3 undergoes

Y. Wu, D. Wu, W. Zhu, X. Chen, Z. Zhou, Z. Liang, S. Ye, G. Zhou
Department of Mechanical Engineering & Materials Science and Engineering Program
State University of New York
Binghamton, NY 13902, USA
E-mail: gzhou@binghamton.edu

M. Li, X. Tong, K. Kisslinger, S. Hwang, D. Zakharov, J. C. Yang
Center for Functional Nanomaterials
Brookhaven National Laboratory
Upton, NY 11973, USA

R. Sharma
Materials Measurement Laboratory
National Institute of Standards and Technology
Gaithersburg, MD 20899, USA

The ORCID identification number(s) for the author(s) of this article can be found under https://doi.org/10.1002/adfm.202519406

DOI: 10.1002/adfm.202519406

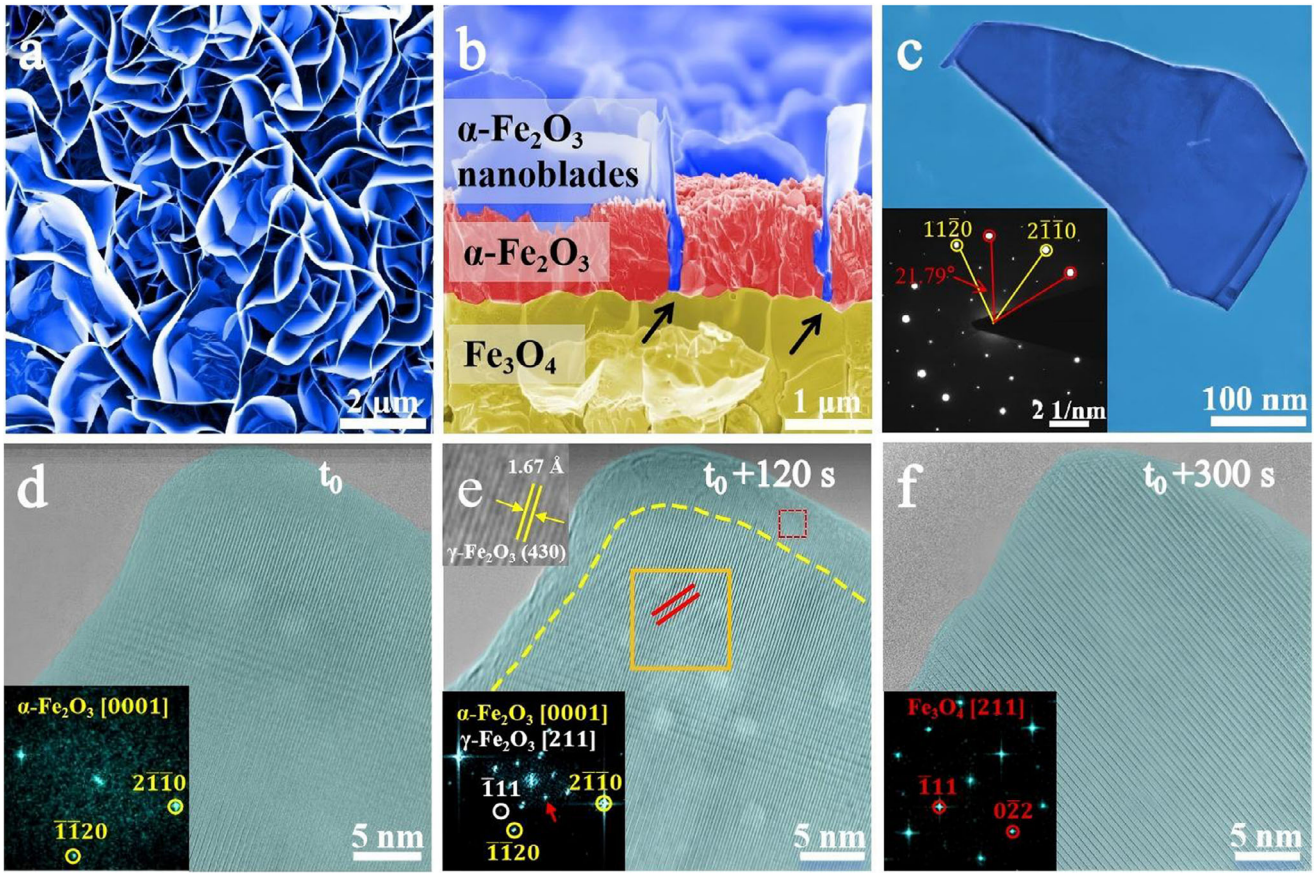

Figure 1. α-Fe_2O_3 nanoblades: morphology, crystal structure, and phase transformations under H_2 reduction (500 °C, 0.5 Pa). a–c) Morphology and crystal phase of as-prepared α-Fe_2O_3 nanoblades formed by thermal oxidation of Fe foil: (a) Top-view SEM image; (b) Cross-sectional SEM image; (c) Low-magnification TEM image of a representative α-Fe_2O_3 nanoblade. The bottom-right inset shows the corresponding nanodiffraction, confirming the α-Fe_2O_3 phase. d–f) In situ TEM images tracking the reduction process in H_2: (d) Pristine α-Fe_2O_3; (e) Intermediate state exhibiting co-existing α-Fe_2O_3 and γ-Fe_2O_3 in a core-shell configuration. Moiré fringes (red lines) appear in the core region due to lattice overlap and double diffraction of the two phases. The yellow dashed line indicates the approximate boundary between the α-Fe_2O_3 core and the γ-Fe_2O_3 shell. Nanopores are visible in the thick region of the γ-Fe_2O_3 shell, while the thinner edge regions remain pore-free. Top-left inset: magnified view of the γ-Fe_2O_3 shell; bottom-left inset: FFT pattern showing distinct reflections of α-Fe_2O_3 (yellow), γ-Fe_2O_3 (white), and their double diffraction (red arrow); (f) Fully reduced to Fe_3O_4, showing a dense, void-free lattice. Inset FFT patterns in d-f confirm the sequential phase transitions (Figure S1 and Table S1, Supporting Information for electron energy loss spectroscopy (EELS) validation).

extensive nanocavity formation driven by vacancy clustering around intrinsic Fe vacancies, whereas Fe_3O_4 remains structurally dense and largely free of porosity throughout reduction. Rather than forming extended vacancy clusters, Fe_3O_4 undergoes a bulk phase transformation to FeO, initiated within the lattice interior. This behavior stands in contrast to the γ-Fe_2O_3 → Fe_3O_4 transformation, which nucleates at the surface and is accompanied by significant porosity within the γ-Fe_2O_3 matrix. These divergent behaviors underscore the critical role of intrinsic vacancy chemistry in controlling reduction pathways and kinetics. By resolving real-time structural evolution during reduction, these results provide mechanistic insights into H_2-based ironmaking and offer design principles for tailoring oxide defect chemistry in applications ranging from metallurgy to catalysis and energy conversion.

2. Results

2.1. In Situ TEM Observations

Figure 1a–c presents the morphology and crystal phase of as-prepared α-Fe_2O_3 nanoblades formed by oxidation of Fe foil at 600 °C in 270 Pa O_2 for 1 h. Figure 1a is a top-view scanning electron microscopy (SEM) image, showing flower-like assemblies of α-Fe_2O_3 nanoblades. Figure 1b is a cross-section SEM image of the oxidized Fe foil, revealing a multilayered oxide scale with an inner Fe_3O_4 layer and an outer α-Fe_2O_3 layer. The surface is covered with vertically oriented α-Fe_2O_3 nanoblades. Black arrows indicate nanoblade roots, which are embedded below the grown α-Fe_2O_3 overlayer. Figure 1c presents a low-magnification TEM image of a representative α-Fe_2O_3 nanoblade.

The bottom-left inset shows the corresponding nanodiffraction pattern, which can be indexed to the corundum structure of α-Fe_2O_3. The diffraction pattern also reveals a bicrystalline structure within the nanoblade.[20,24,32]

Figure 1d–f presents in situ high-resolution transmission electron microscopy (HRTEM) images capturing the dynamic phase evolution of α-Fe_2O_3 nanoblades during reduction at 500 °C and 0.5 Pa H_2. The corresponding fast Fourier transformation (FFT) patterns (lower-left insets) provide crystallographic evidence for sequential phase transformations. Figure 1d corresponds to pristine α-Fe_2O_3, exhibiting no visible Moiré fringes, consistent with a largely homogeneous crystal lattice. Figure 1e captures an intermediate state, where both α-Fe_2O_3 and γ-Fe_2O_3 coexist in a core-shell configuration. The γ-Fe_2O_3 shell forms around the α-Fe_2O_3 core, resulting in overlapping lattice planes that generate weak but discernible Moiré fringes due to double diffraction along the electron beam direction. These fringes serve as a key indicator of phase coexistence. The yellow dashed line outlines the approximate boundary between the core and shell regions. The γ-Fe_2O_3 shell exhibits variable thickness, ranging from ≈1 to ≈5 nm along the edge. In contrast, the absence of such Moiré contrast in Figure 1d confirms the pure α-Fe_2O_3 phase before transformation.

Notably, Figure 1d, e exhibits 1D superlattice features in the top-middle region. These fringes arise from the ordered arrangement of O vacancies. Under H_2 atmospheres, the removal of lattice O generates vacancies that spontaneously self-organize into periodic structures, forming an O-vacancy superlattice.[20,21,33–36] In Figure 1e, nanoscale voids of varying sizes are also observed within the γ-Fe_2O_3 phase—features absent in both α-Fe_2O_3 and Fe_3O_4. These voids are attributed to the aggregation of O vacancies, a process facilitated by the intrinsic Fe vacancies naturally present in the γ-Fe_2O_3 lattice.

Previous studies have confirmed that under reducing conditions, α-Fe_2O_3 undergoes a phase transformation to γ-Fe_2O_3,[20,21,25] involving a structural change from rhombohedral to cubic symmetry. This reduction is driven by progressive removal of lattice O. To maintain the overall Fe:O stoichiometry of 2:3 during this transformation, Fe vacancies are introduced into the γ-Fe_2O_3 lattice to compensate for O loss, thereby stabilizing the resulting spinel structure. Our density functional theory (DFT) calculations (described later) support this mechanism, showing that Fe vacancies serve as energetically favorable nucleation sites for O vacancy aggregation. This synergistic interaction between defects reduces the energy barrier for void formation by destabilizing the γ-Fe_2O_3 lattice, thereby promoting the nucleation of nanoscale voids and accelerating the subsequent phase transformation to Fe_3O_4. In contrast, the absence of such voids in Fe_3O_4 reflects its densely packed structure and greater resistance to vacancy formation and clustering. These observations highlight the critical role of defect interactions in governing phase stability, vacancy dynamics, and transformation pathways during reduction.

Upon exposure to H_2, γ-Fe_2O_3 undergoes progressive O loss, leading to the formation of a high concentration of O vacancies. A portion of these vacancies migrates into the bulk, where they interact with pre-existing Fe vacancies to form nanoscale voids. **Figure** 2a–c shows that the γ-Fe_2O_3 surface undergoes progressive decay and shrinkage during the reduction of γ-Fe_2O_3 at 500 °C and 0.5 Pa H_2. After 547 s, the white dashed line in Figure 2c recedes significantly compared with the original surface in Figure 2a (purple dashed line). This surface degradation is attributed to O vacancies generated by H_2 reacting with lattice O to form H_2O. As vacancies accumulate, the surface becomes unstable, leading to local collapse and Fe atom emission. In the environmental TEM geometry, gas molecules interact with all exposed surfaces; thus, surface-driven vacancy formation refers broadly to accessible surfaces rather than any specific facet orientation.

In addition to driving surface shrinkage, surface-generated vacancies diffuse inward, ultimately leading to porosity in the bulk. Notably, the subsurface (≈10 nm) remains free of porosity throughout extended exposure (≈9 min), while voids are confined to the deeper bulk (Figure 2b,c). The increased distance between the initial surface (purple dashed line) and the marked voids indicates preservation of the porosity-free subsurface layer during surface retreat and void migration. This suggests a dynamic equilibrium where vacancy depletion at the surface is balanced by replenishment from the bulk, suppressing clustering near the surface but allowing accumulation deeper inside. Once the supersaturation threshold is exceeded—facilitated by intrinsic Fe vacancies—voids nucleate and coalesce, leading to cyclic vacancy migration and clustering and ultimately a porous microstructure. This progression of surface decay and bulk porosity is consistently observed across multiple regions and samples (Figure S2, Supporting Information).

Instead of collapsing into voids, the progressive accumulation of O vacancies in the surface regions triggers a localized, surface-mediated phase transformation to Fe_3O_4. This mechanism is supported by the formation of Fe_3O_4 surface bulges on γ-Fe_2O_3 nanowires following reduction in H_2 (Figure S3, Supporting Information). These surface features mark the nucleation sites of Fe_3O_4, confirming that the transformation initiates preferentially at the surface rather than in the bulk. This observation aligns with our previous study[21] and highlights the critical role of rapid surface O depletion in driving the γ-Fe_2O_3 → Fe_3O_4 transition. The spatial separation of bulk void formation and surface phase transformation reflects distinct pathways of vacancy evolution at the surface and in the bulk under reducing conditions.

Figure 2d–h presents in situ HRTEM images capturing the dynamic evolution of vacancy clusters (voids) in the γ-Fe_2O_3 bulk under the same reducing conditions. Initially irregularly shaped voids gradually develop into faceted geometries bounded by low-index {111} and {110} planes (inset FFT, Figure 2h), which are known to possess lower surface energies,[37,38] consistent with negative crystals that mimic the host lattice symmetry. Such faceting reflects anisotropic vacancy diffusion, clustering, and lattice dissolution along low-energy planes,[39–42] in accordance with Wulff construction principles.

The observations reveal three dynamic behaviors: nucleation, growth, and dissolution. As shown in Figure 2d–g, two voids of similar initial size evolve differently—one grows then dissolves within 274 s, while the other gradually shrinks—highlighting local differences in vacancy supply. Void growth occurs when the surrounding lattice is enriched in vacancies, whereas dissolution arises when the local concentration drops below the stability threshold. When the vacancy concentration exceeds supersaturation, new voids nucleate spontaneously.

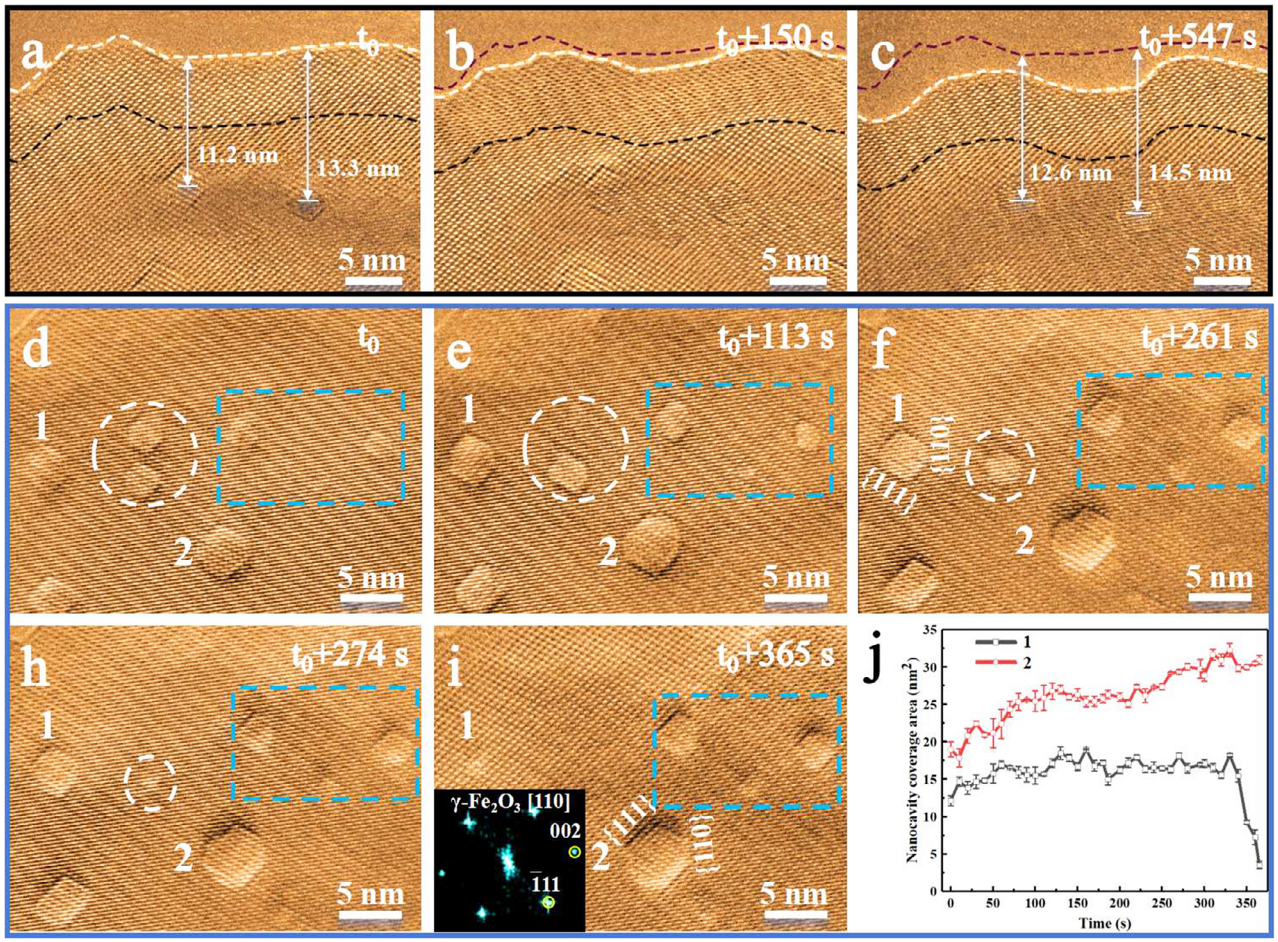

Figure 2. Dynamic evolution of surface morphology and vacancy clusters in γ-Fe_2O_3 during reduction at 500 °C under 0.5 Pa H_2. a–c) Sequential HRTEM images (Supplementary in situ TEM Video S1, Supporting Information) showing gradual surface shrinkage and the absence of pore formation in the subsurface region (≈10 nm beneath the outermost surface). White dashed lines trace the evolving surface profile, while the purple dashed lines mark the initial surface position at t_0. Black dashed lines approximately delineate the boundary between the porosity-free subsurface layer and the deeper bulk region where nanoscale voids form. d–h) Time-resolved HRTEM images (Supplementary in situ TEM Video S2, Supporting Information) capturing the nucleation, growth, migration, and dissolution of vacancy clusters in the γ-Fe_2O_3 bulk. Two representative regions are highlighted: white dashed circles track dissolving vacancy clusters, while blue dashed rectangles follow growing vacancy clusters. Inset in (h): corresponding FFT pattern. i) Temporal evolution of vacancy clusters 1 and 2 labeled in (d-h).

This mechanism is illustrated in the blue-dashed region (Figure 2d–g): two preexisting voids intensify in contrast as they grow, while a new void nucleates ≈113 s and expands, indicating 3D vacancy aggregation. The coexistence of new and growing voids contradicts classical Ostwald ripening, where larger clusters grow at the expense of smaller ones, and instead underscores the central role of vacancy flux in the oxide lattice.[43–45] Quantitative analysis (Figure 2i) further shows contrasting trajectories: void 1 fluctuates then dissolves, while void 2 grows steadily, accompanied by nucleation of smaller voids nearby. These behaviors reflect the delicate balance of vacancy supply, with growth, nucleation, and dissolution governed by local concentration dynamics rather than equilibrium coarsening. Importantly, the FFT in Figure 2h confirms that the γ-Fe_2O_3 lattice remains stable without transformation to Fe_3O_4.

Figure 3 presents in situ high-resolution (HR) TEM images capturing the atomic-scale structural evolution during the reduction of γ-Fe_2O_3 to Fe_3O_4 at 500 °C and 0.5 Pa H_2. In Figure 3a–e, two distinct lattice regions coexist, separated by an interface exhibiting slight Moiré fringes, indicative of overlapping lattices in the interface region. The corresponding FFTs (insets in Figure 3a,b) confirm cubic symmetry in both regions, consistent with the γ-Fe_2O_3 and Fe_3O_4 phases, respectively. In agreement with observations in Figure 1e,f, the γ-Fe_2O_3 region (upper left) contains nanoscale voids (appearing as bright contrast). In contrast, the Fe_3O_4 region (lower right) displays uniform contrast with no porosity, indicating minimal O vacancy formation and aggregation in this phase. These observations suggest that the reduction is predominantly localized within the γ-Fe_2O_3 phase at this stage. This interpretation is further supported by DFT modeling (discussed later), showing that γ-Fe_2O_3 has a lower O vacancy formation energy than Fe_3O_4, making it more susceptible to reduction.

The cyan dashed lines in Figure 3a–e mark the initial γ-Fe_2O_3/Fe_3O_4 interface position observed in Figure 3a, while the white dashed lines indicate this initial position in subsequent

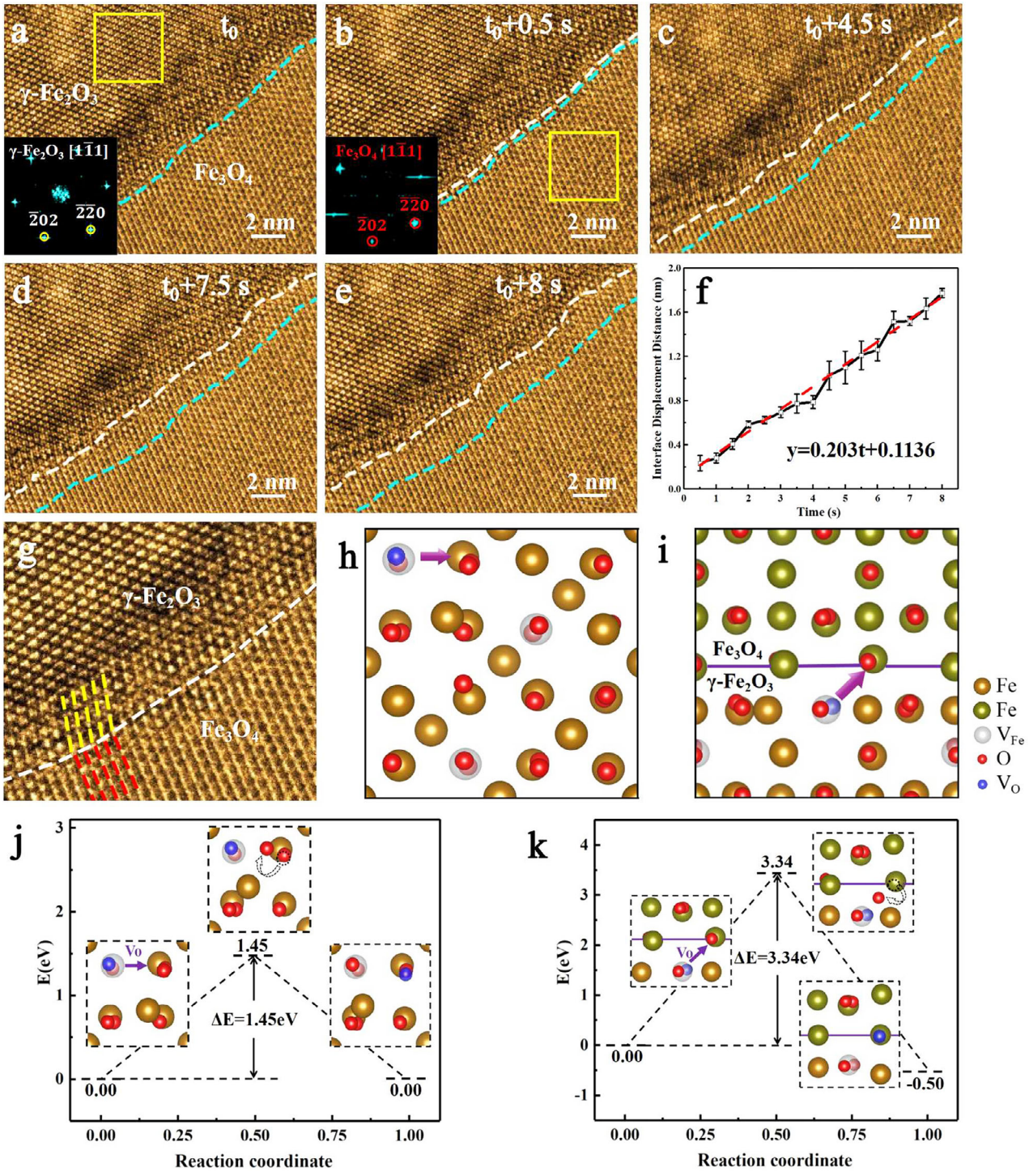

Figure 3. In situ HRTEM imaging of the γ-Fe_2O_3 to Fe_3O_4 transformation during reduction at 500 °C and 0.5 Pa H_2. a–e) Time-resolved HRTEM images (Supplementary in situ TEM Video S3, Supporting Information) capturing dynamic γ-Fe_2O_3/Fe_3O_4 interface migration during the topotactic phase transformation. Bottom-left insets in (a,b) correspond to FFT patterns of the yellow-boxed regions, confirming phase identification of γ-Fe_2O_3 and Fe_3O_4. White dashed lines track the advancing γ-Fe_2O_3/Fe_3O_4 interface, while the cyan dashed lines mark the initial interface position at t_0. f) Time-dependent interface displacement distance, with error representing standard deviation uncertainties based on multiple measurements at different locations. g) Zoomed-in HRTEM image of the γ-Fe_2O_3/Fe_3O_4 interface, showing tilted yet continuous one-to-one lattice plane matching across the interface. h) Atomic model illustrating the nearest O diffusion pathway within the γ-Fe_2O_3 bulk, viewed along the [100] direction. i) Atomic model showing the nearest O migration pathway from the γ-Fe_2O_3 lattice toward the γ-Fe_2O_3/Fe_3O_4 interface, viewed along [100]. j,k) NEB calculations of the diffusion energy barriers for O vacancy migration within the γ-Fe_2O_3 (j) and toward the γ-Fe_2O_3/Fe_3O_4 interface (k), corresponding to the pathways depicted in (h) and (i), respectively.

images to track the interface migration over time. A comparison of these positions reveals that the interface advances ≈2 nm into the γ-Fe_2O_3 region over an 8 s interval, indicating that γ-Fe_2O_3 serves as an intermediate that gradually reduces to Fe_3O_4. This interfacial transformation is driven by the reaction of lattice O with adsorbed H at the γ-Fe_2O_3 surface, producing H_2O and generating O vacancies. Some of these vacancies contribute to surface shrinkage (Figure 2a–c) or Fe_3O_4 nucleation (Figure S3, Supporting Information), while others migrate inward, promoting nanovoid formation in the bulk or advancing the γ-Fe_2O_3/Fe_3O_4 interface. This surface-to-bulk vacancy migration is consistent with prior reports in related oxide systems.[46–48] The prominent void formation observed in the γ-Fe_2O_3 region suggests that excess O vacancies accumulate and cluster within the γ-Fe_2O_3 lattice, reducing their availability for the γ-Fe_2O_3/Fe_3O_4 interface migration. This implies that the clustering of O vacancies within the γ-Fe_2O_3 bulk competes with vacancy flux to the γ-Fe_2O_3/Fe_3O_4 interface, thereby impeding the overall interface propagation and slowing the phase transformation kinetics.

Figure 3f quantifies the displacement of the γ-Fe_2O_3/Fe_3O_4 interface over time, revealing a linear progression at a rate of ≈0.2 nm s^{-1}. This linearity suggests that the transformation kinetics are governed by interfacial reaction processes, rather than by bulk diffusion. In a diffusion-limited process, one would expect a non-linear acceleration in interface migration as the γ-Fe_2O_3 region shrinks and diffusion paths shorten. Additional support for interface-controlled kinetics comes from the persistent presence of voids in the γ-Fe_2O_3 region. These voids arise from the clustering of excess O vacancies that are not fully consumed at the advancing interface. If bulk diffusion were the rate-determining step, we would expect a steady and uniform flux of O vacancies migrating from the γ-Fe_2O_3 region toward the γ-Fe_2O_3/Fe_3O_4 interface, where they would be consumed to sustain interfacial Fe_3O_4 growth. Under this scenario, significant vacancy accumulation and void formation within the γ-Fe_2O_3 bulk would not occur. However, our in situ observations clearly show extensive nanovoid formation in the γ-Fe_2O_3 interior, indicating that O vacancies are not rapidly annihilated at the interface. This supports the conclusion that bulk diffusion is not the rate-limiting step and that the interfacial reaction kinetics govern the overall transformation. Therefore, the slower kinetics of the interfacial reaction impede this vacancy annihilation, leading to a buildup of excess O vacancies within the γ-Fe_2O_3 bulk. Once these vacancies become supersaturated, they subsequently aggregate into nanoscale voids. Thus, the combination of (i) the linear interface displacement and (ii) the formation of voids in γ-Fe_2O_3, observed consistently across multiple independent samples (Figure S4, Supporting Information), provides compelling evidence that the phase transformation from γ-Fe_2O_3 to Fe_3O_4 is governed by interfacial reactivity rather than bulk vacancy diffusion.

Figure 3g presents a zoomed-in view of the γ-Fe_2O_3/Fe_3O_4 interface, revealing a coherent, one-on-one alignment of the (110) lattice planes across the interface, despite a slight angular mismatch. In situ HRTEM imaging (Figure 3a–e) confirms that this coherent interface configuration is maintained throughout the phase transformation, indicating a topotactic relationship—where the crystallographic orientation is preserved during the structural reorganization from γ-Fe_2O_3 to Fe_3O_4.

Figure 3h illustrates the migration pathways of O vacancies within the γ-Fe_2O_3 bulk, while Figure 3i shows an atomic model of the γ-Fe_2O_3/Fe_3O_4 interface constructed based on the experimental structure in Figure 3g. In building this model, the Fe sublattice is chosen as the structural framework, since γ-Fe_2O_3 can be regarded as a defect derivative of Fe_3O_4 that preserves the same inverse spinel Fe framework but incorporates ordered Fe vacancies at the octahedral sites. This model highlights that the Fe sublattices remain structurally continuous across the interface, implying that the phase transformation requires only the removal of O from the γ-Fe_2O_3 without disrupting or rearranging the Fe framework, consistent with experimentally observed coherent the γ-Fe_2O_3/Fe_3O_4 interface (Figure 3g). These diffusion pathways shown in Figure 3h,i represent the shortest routes for O vacancy migration between neighboring lattice O sites. The phase transformation proceeds via the loss of lattice O at the interface, reducing the local O content to match the Fe_3O_4 stoichiometry. This is accomplished through the migration of O vacancies from the adjacent γ-Fe_2O_3 lattice toward the interface, which is coupled with a compensatory migration of lattice O from the interfacial region back into the γ-Fe_2O_3 bulk. This exchange facilitates the interfacial reduction of γ-Fe_2O_3 into Fe_3O_4, while preserving the Fe lattice continuity.

Based on the two models in Figure 3h,i, we perform nudged elastic band (NEB) calculations to evaluate the energy barriers associated with the O vacancy diffusion in two key regions: within the γ-Fe_2O_3 bulk and from the γ-Fe_2O_3 lattice toward the γ-Fe_2O_3/Fe_3O_4 interface. These calculations aim to uncover the atomic-level origin of the interfacial reactivity that governs the rate-limiting step in the phase transformation. As shown in Figure 3j, the diffusion barrier for O vacancies within the bulk γ-Fe_2O_3 is calculated to be 1.45 eV, indicating relatively facile migration in the interior of the lattice. In contrast, Figure 3k shows that the energy barrier for O vacancy migration from the γ-Fe_2O_3 bulk to the interface is significantly higher, at 3.34 eV. This substantial increase in activation energy near the interface suggests that O vacancy transport becomes increasingly hindered as it approaches the γ-Fe_2O_3/Fe_3O_4 boundary. The pronounced difference in diffusion barrier supports the interpretation that the phase transformation is not limited by bulk vacancy diffusion but is instead governed by interfacial reaction kinetics. This mechanistic insight is consistent with experimental observations of linear interface migration and vacancy accumulation in the γ-Fe_2O_3 bulk, providing a coherent explanation for the interface-controlled reduction behavior observed during the γ-Fe_2O_3 to Fe_3O_4 transformation.

Figure 4 shows in situ TEM observations that further clarify the difference in H_2-driven phase transformation pathways between γ-Fe_2O_3 and Fe_3O_4. Two distinct features are revealed during the reduction: (1) Pore formation: A region enclosed by white dashed lines shows the gradual development of a cavity within Fe_3O_4. Despite the growth of this pore, the surrounding lattice maintains well-defined Fe_3O_4 fringes and interplanar spacings, with no observable lattice distortion or contraction. This consistency confirms that the contrast arises from a structural void rather than a phase transformation, identifying the feature as a true pore. (2) FeO nucleation: In a nearby region (outlined in black), a different type of contrast emerges, marked by a reduction in interplanar spacing and a change in lattice symmetry. FFT

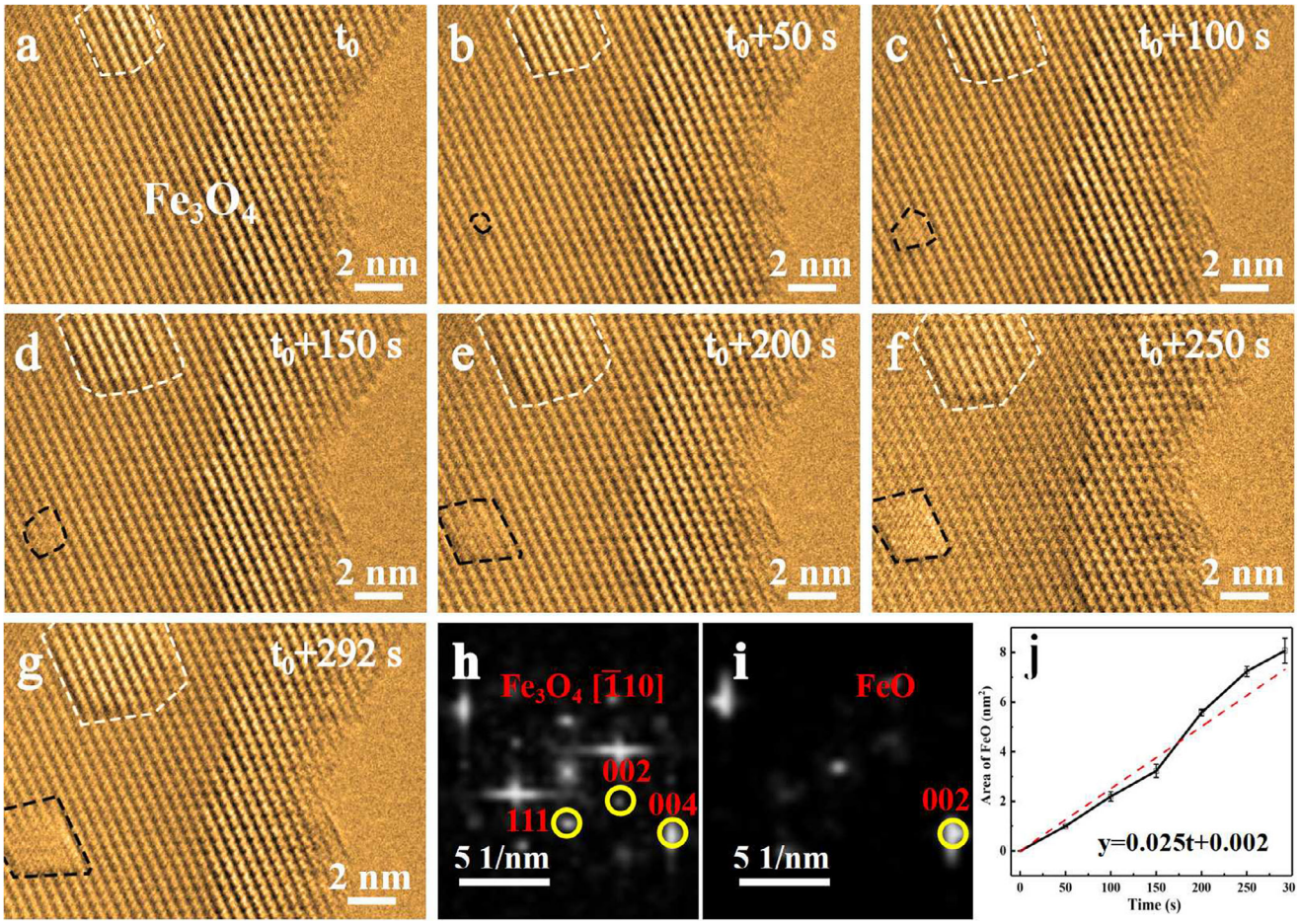

Figure 4. Dynamic evolution of FeO nucleation and pore formation within Fe_3O_4 bulk during reduction at 500 °C under 0.5 Pa H_2. a–g) Time-resolved HRTEM images (Supplementary in situ TEM Video S5, Supporting Information) showing the gradual development of a structural pore (outlined in white) and the nucleation and growth of FeO (outlined in black) in a separate nearby region. h,i) Corresponding FFT patterns taken from the pore (h) and FeO (i) regions, respectively. j) Temporal evolution of the FeO size, extracted from the black-marked region in (a–g).

analysis (Figure 4h,i) further distinguishes the two regions: the pore region shows {002} and {111} reflections consistent with Fe_3O_4, while the FeO region lacks these reflections and instead displays only {004} spots—consistent with the rock-salt structure of FeO. These differences confirm the nucleation and growth of FeO within the Fe_3O_4 lattice. These side-by-side observations allow for differentiating between structural voids and phase transitions.

The small difference (≈0.05 Å) between the d-spacings of Fe_3O_4 (004) and FeO (002) can complicate phase identification when relying solely on interplanar spacing. Our phase assignment is thus based on multiple lines of evidence: lattice spacing changes, real-time contrast evolution, FFT patterns, and local crystallinity. The pore region preserves Fe_3O_4 lattice features, while the FeO region displays both a distinct lattice spacing contraction and altered diffraction symmetry.

As shown in Figure 4, FeO formation within Fe_3O_4 initiates in the lattice interior rather than at free surfaces or pore boundaries, as no FeO is observed at side facets or within the pore. While minor porosity can develop in Fe_3O_4 under reducing conditions, it remains sparse and does not facilitate FeO nucleation. This contrasts with γ-Fe_2O_3, which undergoes surface-initiated Fe_3O_4 nucleation (Figure S3, Supporting Information) and exhibits extensive pore formation during reduction (Figures 1–3). These observations confirm that Fe_3O_4 is intrinsically more resistant to vacancy aggregation than γ-Fe_2O_3. Although limited porosity may occur, Fe_3O_4 maintains a denser structure and follows a distinct reduction pathway—undergoing bulk-initiated FeO formation rather than surface-driven transformations.

Figure 4j presents the measured growth rate of the projected FeO area during the Fe_3O_4-to-FeO transformation, yielding ≈0.025 $nm^2\ s^{-1}$ based on linear fitting. For comparison, the growth rate of Fe_3O_4 during the γ-Fe_2O_3-to-Fe_3O_4 transformation is 5.89 $nm^2\ s^{-1}$ (Figures S5, Supporting Information). It is important to note that transformation kinetics are governed not only by growth rates but also by the nucleation mechanism. The γ-Fe_2O_3-to-Fe_3O_4 transition initiates at the surface (Figure S3, Supporting Information), whereas the Fe_3O_4-to-FeO transformation nucleates within the bulk (Figure 4), reflecting fundamentally different vacancy dynamics and transport behaviors. Specifically, γ-Fe_2O_3 exhibits vacancy clustering and localized void formation, which restricts phase transformation to the interface

region, while in Fe_3O_4, vacancies are more uniformly distributed, allowing smoother bulk transformation.

Although a fully quantitative comparison of transformation kinetics is limited by experimental constraints—such as sample drift, gas pressure fluctuations, H_2 dosing delay, and limited field of view—the qualitative differences in nucleation pathways, vacancy distribution, and interface propagation strongly support our conclusion: that vacancy dynamics—particularly the contrast between clustering in γ-Fe_2O_3 and bulk diffusion in Fe_3O_4—play a decisive role in governing the reduction pathway and rate.

Finally, we emphasize that the observed differences between γ-Fe_2O_3 and Fe_3O_4 reduction behavior in our in situ TEM experiments are driven by the H_2 atmosphere, not by electron beam effects. This is confirmed by beam-blanking control experiments (Figure S6, Supporting Information), which show comparable reduction behavior with and without electron beam exposure (flux $\approx 3.8 \times 10^5$ $e^-/nm^2 \cdot s$; Figure 1–3). Additional validation is provided by ex-situ reduction experiments (described in Section 2.2), which reproduce the same phase-dependent morphological differences—namely, porous γ-Fe_2O_3 and dense, pore-free Fe_3O_4—as observed in the in situ studies.

2.2. Ex-Situ STEM Imaging

Ex-situ high-angle annular dark-field scanning TEM (HAADF-STEM) further corroborates the in situ TEM results by comparing γ-Fe_2O_3 and Fe_3O_4 formed during the reduction of α-Fe_2O_3 at 500 °C under ≈700 Pa H_2 in a vacuum chamber. HAADF-STEM, which provides contrast based on atomic number and sample thickness, reveals pronounced porosity in γ-Fe_2O_3, visible as darker regions corresponding to localized thinning (**Figure 5a**). Compared to the ≈2–5 nm voids observed in in situ TEM experiments (Figures 1–3), the voids in the ex-situ samples are significantly larger—spanning several tens of nanometers. This size difference is attributed to the higher H_2 pressure during ex-situ reduction, which promotes more extensive O vacancy generation and aggregation, resulting in larger nanovoids.

To confirm that these voids reside within the γ-Fe_2O_3 bulk rather than on the surface—an ambiguity in projection-based HAADF-STEM imaging, we perform secondary electron (SE) imaging, which is more sensitive to surface topography. The STEM-SE image in Figure 5b, taken from the same region as Figure 5a, shows no surface depressions or pits at the locations corresponding to the voids seen in HAADF-STEM, confirming that the observed porosity originates from voids with the γ-Fe_2O_3 bulk.

These porous features in γ-Fe_2O_3 are further validated by corresponding energy-dispersive X-ray spectroscopy (EDS) maps (Figure S7a–c, Supporting Information), which show concurrent depletion of Fe and O within the cavity regions—indicative of void formation via aggregation of Fe and O vacancies during reduction. In contrast, Fe_3O_4 exhibits uniform HAADF contrast with no evidence of porosity, consistent with EDS maps (Figure S7d–f, Supporting Information) that display homogeneous Fe and O distribution. These contrasting microstructures between γ-Fe_2O_3 and Fe_3O_4 are consistently observed across multiple independently reduced samples (Figures S8 and S9, Supporting Information).

Figure 5c–h presents ex-situ HAADF-STEM characterization of Fe_3O_4 and γ-Fe_2O_3 formed from the in situ TEM experiments. These images provide direct structural insight into a distinction between the two phases: while the O sublattice is invisible in HAADF-STEM, the Fe sublattice is clearly resolved, revealing that γ-Fe_2O_3 contains intrinsic Fe vacancies, whereas Fe_3O_4 maintains a fully occupied Fe sublattice.

In the Fe_3O_4 region (Figure 5c,d), the atomic structure remains uniform and intact, exhibiting consistent Z-contrast across the images, without signs of vacancy clusters. This homogeneity indicates a well-ordered arrangement of both Fe and O atoms in the oxide lattice. Intensity line profiles taken from four randomly selected atomic planes further confirm this structural uniformity, each exhibiting consistent column intensities (Figure 5e). This consistency confirms the conclusion that Fe_3O_4 lacks significant Fe vacancy concentration and preserves an intact cation sublattice.

In contrast, the γ-Fe_2O_3 region displays localized reductions in HAADF intensity (Figure 5f), indicative of nanoscale voids. These features correspond to vacancy clusters composed of both Fe and O vacancies, rather than O-deficiency alone. This interpretation is supported by the high-resolution HAADF image of the pore region (bottom-left inset of Figure 5f), which shows no discernible lattice distortion—implying that the Fe sublattice itself remains ordered locally, despite the presence of significant Fe vacancies. If only O vacancies are present, the resulting lattice strain or relaxation would likely manifest as visible distortions in the atomic columns.

To further confirm the presence of intrinsic Fe vacancies, HAADF-STEM imaging is performed in pore-free regions to avoid contrast artifacts. As shown in Figure 5g,h, intensity profiles across four randomly selected atomic planes reveal pronounced variations in the brightness of adjacent atomic columns within the same layer. Given the relatively uniform thickness, these intensity fluctuations cannot be attributed to geometric or thickness-related contrast effects. Instead, they reflect local variations in atomic occupancy, consistent with a high concentration of intrinsic Fe vacancies in the γ-Fe_2O_3 lattice.

2.3. DFT Modeling

As shown in Figure 2a–c, the γ-Fe_2O_3 surface undergoes progressive recess during reduction. This behavior is driven by the formation of O vacancies, initiated by the surface reaction of lattice O with adsorbed H to form H_2O. The desorption of H_2O leaves behind O vacancies, which contribute to surface shrinkage or migrate into the lattice. The preferential formation of voids in γ-Fe_2O_3, as opposed to the denser Fe_3O_4, suggests that O vacancies form more readily on the γ-Fe_2O_3 surface. This is supported by DFT calculations, which show significantly lower O vacancy formation energies on γ-Fe_2O_3(100) (1.87–2.62 eV) compared to Fe_3O_4(100) (2.71–3.46 eV), depending on the local surface coordination environment (Figure S10, Supporting Information).

The absence of Fe sublattice defects in Fe_3O_4 highlights the structural origin of void formation observed exclusively in γ-Fe_2O_3 during reduction. The spinel structure of Fe_3O_4 accommodates both Fe^{2+} and Fe^{3+} cations in a compact and energetically stable configuration, which effectively suppresses the

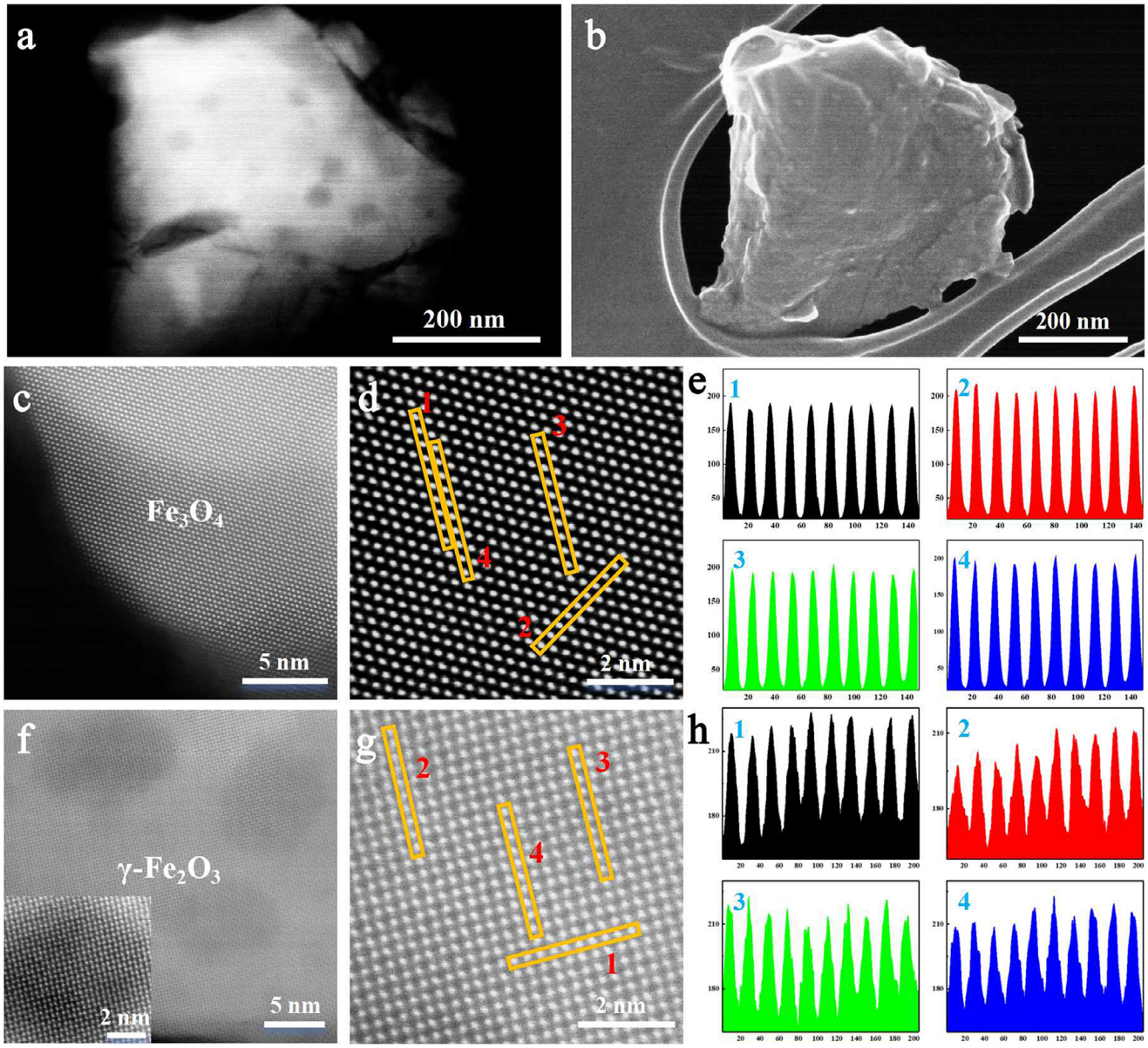

Figure 5. Ex-situ STEM characterization of γ-Fe_2O_3 and Fe_3O_4 formed during reduction of α-Fe_2O_3 at 500 °C. a,b) HAADF-STEM image (a) and corresponding surface-sensitive STEM-SE image (b) of γ-Fe_2O_3 reduced under ≈700 Pa H_2 in a vacuum chamber. The absence of surface pits in (b) confirms that the dark contrast regions in (a) originate from internal nanovoids rather than surface features. c–h) HAADF-STEM imaging of γ-Fe_2O_3 and Fe_3O_4 formed under 0.5 Pa H_2 in in situ TEM experiments. (c) Low-magnification STEM-HAADF imaging of Fe_3O_4, (d) Atomically resolved image the region in (c), (e) Corresponding intensity line profiles from representative atomic layers indicated in (d), showing uniform column intensities consistent with an intact Fe sublattice and negligible Fe vacancy concentration. (f) Low-magnification STEM-HAADF image of γ-Fe_2O_3, inset shows a magnified view of a nanovoid region, (g) Atomically resolved HAADF-STEM image of the γ-Fe_2O_3 lattice away from the void region, (f) Corresponding intensity line profiles from representative atomic layers marked in (g), showing significant site-to-site variations in atomic column intensity, indicative of a defective Fe sublattice with a high concentration of Fe vacancies.

formation and clustering of cation vacancies. In contrast, γ-Fe_2O_3 possesses an inherently defective Fe sublattice due to its nonstoichiometric composition and partially occupied cation sites. In γ-Fe_2O_3, intrinsic Fe vacancies act as energetically favorable sinks that stabilize additional vacancies, promoting stochastic vacancy clustering and nanovoid formation during reduction. By contrast, Fe_3O_4 lacks stabilizing Fe vacancies, so O vacancies aggregate less readily, suppressing porosity. To elucidate the atomic-scale mechanisms underlying this contrasting behavior—specifically, the resistance of Fe_3O_4 to vacancy clustering and the propensity for vacancy aggregation in γ-Fe_2O_3, we perform DFT calculations. These simulations probe the thermodynamic stability, migration barriers, and interaction energetics of Fe and O vacancies in both oxides, providing critical insights into the driving forces and kinetic pathways that govern vacancy behavior during reduction.

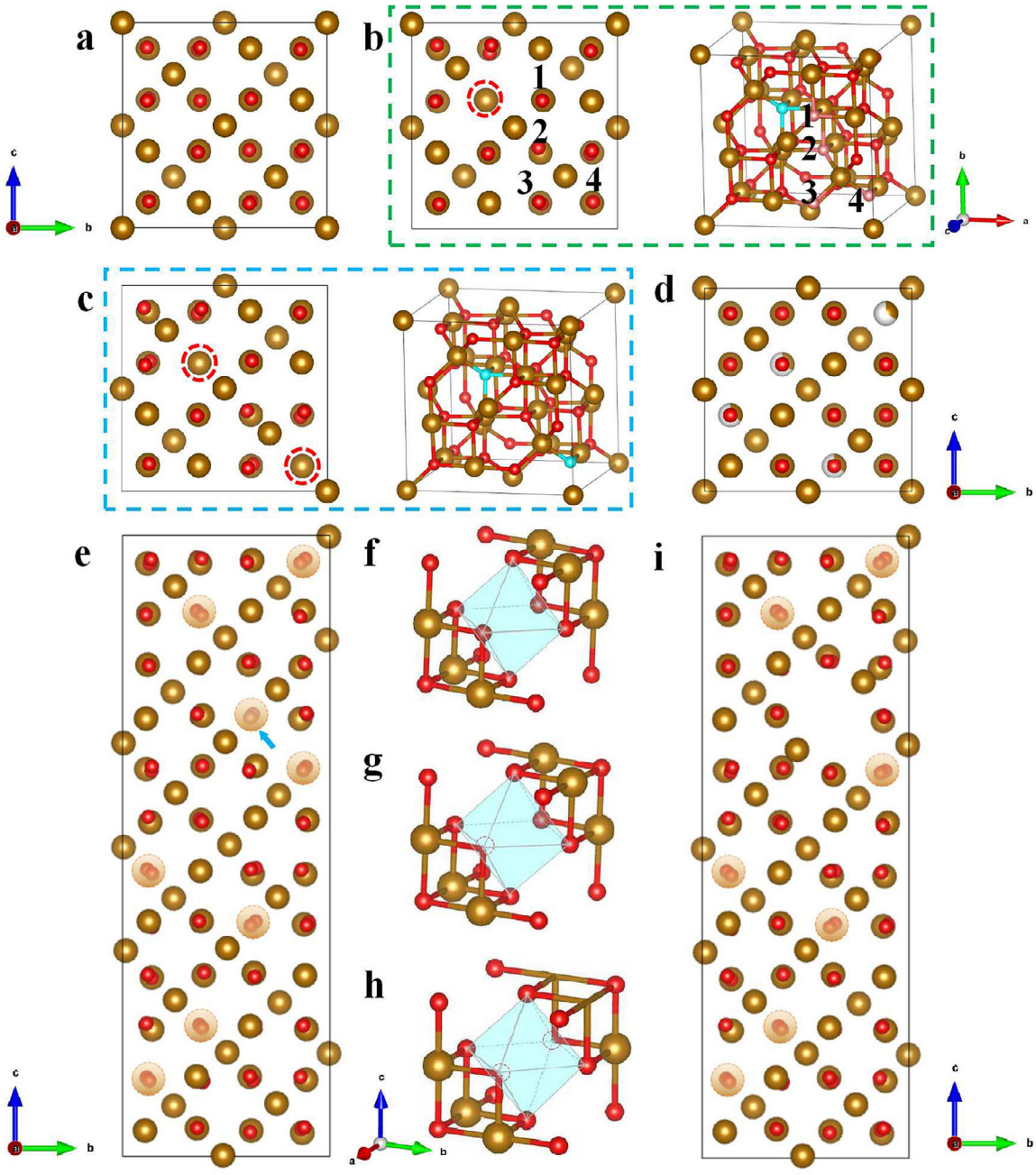

Figure 6. Atomic-scale modeling of vacancy dynamics in Fe_3O_4 and γ-Fe_2O_3. a–c) DFT-optimized structures of Fe_3O_4: (a) Pristine spinel lattice. (b) Di-O vacancy configurations: the initial O vacancy is marked by a red dashed circle in the projection view (left) and by a blue sphere in the perspective view (right); the second O vacancy is positioned at four distinct sites (1–4). (c) Relaxed structure of the most favorable di-O vacancy configuration, shown in both projection (left) and perspective (right) views. d) Structural model of γ-Fe_2O_3 model featuring a partially disordered Fe sublattice, with intrinsic Fe vacancies indicated by white spheres. e) Supercell of γ-Fe_2O_3 showing Fe vacancy site (orange circles) and candidate O vacancy formation site (blue arrow). f–h) Sequential 3D schematics illustrating vacancy cluster formation in γ-Fe_2O_3, O vacancies (red dashed circles) preferentially form and aggregate around an intrinsic Fe vacancy (blue octahedral void). i) Final relaxed configuration of the vacancy cluster within the γ-Fe_2O_3 supercell. Yellow and red spheres represent Fe and O atoms, respectively.

Magnetite (Fe_3O_4) is a ferrimagnetic oxide with the chemical formula $(Fe^{3+})_8[Fe_8^{2+}Fe_8^{3+}]O_{32}$, where Fe ions in parentheses occupy tetrahedral sites and those in square brackets occupy octahedral sites (**Figure 6a**).[43–45] To investigate why Fe_3O_4 does not form vacancy clusters, we first compute the formation energy of an isolated O vacancy in its bulk lattice. Due to the high symmetry of the spinel structure, all O sites are crystallographically equivalent. As indicated by the dashed circle in Figure 6b, the formation energy for a single O vacancy is calculated to be 3.5 eV. Building on this, we evaluate the formation energies of a second O vacancy

introduced at four distinct sites (O_1–O_4) are in the presence of the initial vacancy. The computed energies decrease in the order O_3 (3.62 eV) > O_2 (3.41 eV) > O_1 (3.02 eV) > O_4 (2.71 eV), identifying O_4 as the most favorable site for a second O vacancy (Figure 6c). 3D structural views of the O vacancies in the Fe_3O_4 further illustrate this trend: although an initial O vacancy (blue sphere) preferentially promotes subsequent vacancy formation at the O_4 site, their spatial separation remains substantial (≈6 Å). Moreover, the absence of intrinsic Fe vacancies in the Fe_3O_4 lattice renders O vacancy clustering energetically unfavorable. This dual limitation—insufficient O vacancy proximity and no intrinsic Fe vacancies to stabilize vacancy clusters—explains the experimentally observed void-free microstructure of Fe_3O_4 under reducing conditions.

In contrast to Fe_3O_4, γ-Fe_2O_3 (maghemite) shares a similar spinel-type framework but incorporates ≈8/3 Fe vacancies per unit cell, as illustrated in Figure 6d. These vacancies—represented by a white sphere indicating a 2/3 probability of vacancy occupation at given Fe sites—predominantly reside at octahedral sites. This defect-rich configuration yields a nonstoichiometric formula of $(Fe^{3+})_8[Fe^{3+}{}_5/_6\ \square_1/_6]_{16}O_{32}$, where □ denotes a cation vacancy.[49,50] Unlike the defect-free Fe sublattice of Fe_3O_4, the Fe^{3+} vacancies in γ-Fe_2O_3 are only partially ordered. Rather than forming a periodic arrangement, these intrinsic Fe vacancies are typically disordered, introducing structural instability and enabling dynamic defect behavior—particularly under reducing conditions.

To explain the possible ordered configuration, Oosterhout and Rooijmans[51,52] proposed a tetragonal superstructure (with a c/a ratio of ≈3) in which Fe^{3+} vacancies are fully ordered and restricted to Wyckoff 4b sites. In this ideal structure, the uniform distribution of Fe^{3+} cations and vacancies minimizes Coulombic repulsion and enhances lattice stability. However, such ordering is rarely achieved under practical conditions. In reality, the disordered Fe sublattice in γ-Fe_2O_3 provides abundant energetically favorable sites for O vacancy formation and clustering.

Figure 6e depicts a model of the ordered superstructure of γ-Fe_2O_3, where intrinsic Fe vacancies (indicated by semi-transparent orange spheres) are localized at octahedral sites, further illustrated in the 3D view of Figure 6f. To investigate O vacancy formation near an Fe vacancy, DFT calculations are performed for the O sites adjacent to the Fe vacancy (indicated by the blue arrow in Figure 6e). The computed formation energy for a single O vacancy at this site (Figure 6g) is 3.01 eV. An adjacent lattice O site (Figure 6h) is found to be the most favorable for a second O vacancy, with a lower formation energy of 2.92 eV. The proximity of a pre-existing Fe vacancy thus significantly lowers the energy barrier for nearby O vacancy formation, promoting their spatial aggregation. As illustrated in Figure 6i, this synergistic interaction between Fe vacancies (intrinsic to γ-Fe_2O_3) and nearby O vacancies enables the nucleation of a vacancy cluster or void, characterized by the absence of both Fe and O ions.

This vacancy clustering behavior is absent in Fe_3O_4. There, the relatively high O vacancy formation energy (≈3.5 eV) and the lack of intrinsic Fe vacancies create a thermodynamic barrier that inhibits the development of vacancy clusters. Conversely, γ-Fe_2O_3 contains inherent Fe vacancies that act as nucleation sites and simultaneously lower the formation energy of nearby O vacancies, thereby promoting their aggregation. This contrasting difference arises from their distinct structural characteristics: the mixed-valence of Fe^{2+}/Fe^{3+} spinel structure of Fe_3O_4 stabilizes the cation sublattice and resists O vacancy formation and aggregation, while the Fe^{3+}-only framework naturally accommodates Fe vacancies, enabling cooperative vacancy clustering and void formation.

3. Discussion

This study demonstrates that the aggregation of vacancies in γ-Fe_2O_3 leads to the formation of nanopores, a phenomenon with significant implications for hydrogen-based direct reduction in steelmaking. Thermodynamically, the spontaneous clustering of Fe and O vacancies reduces the overall concentration of isolated O vacancies by incorporating them into stable voids. This effectively diminishes the lattice O deficiency and consequently slows the progression of γ-Fe_2O_3 to lower oxides such as Fe_3O_4. Beyond thermodynamics, this nanoscale porosity introduces critical kinetic constraints. The resulting nanopores can act as entrapment zones for H_2O, the reaction product of lattice O and H_2, disrupting its desorption and transport away from the reaction front.

Under ideal conditions, H_2O produced during reduction readily desorbs from the surface and diffuses away, allowing sustained progress of the reduction. However, in γ-Fe_2O_3, the formation of internal nanopores creates confined environments that act as nanoscale reactors. These pores trap H_2O molecules, significantly impeding their outward diffusion.[52–54] This localized entrapment generates kinetic bottlenecks, increases the partial pressure of H_2O near the reaction front, and suppresses further removal of lattice O, causing the actual reaction kinetics to deviate from thermodynamic expectations.

In contrast, Fe_3O_4 exhibits markedly behavior under H_2 reduction. Its spinel structure lacks intrinsic Fe vacancies and has a significantly higher O vacancy formation energy compared to γ-Fe_2O_3. As a result, vacancy clustering is suppressed, and O vacancies remain more uniformly distributed throughout the lattice. This uniformity enables a progressive and delocalized depletion of lattice O—a necessary condition for the bulk-initiated FeO nucleation (Figure 4).

Although our in situ environmental TEM experiments are conducted at a low H_2 pressure (≈0.5 Pa), we assess the pressure dependence of this phase behavior through complementary ex-situ reduction experiments at the same temperature (500 °C) but under higher pressures (≈700 Pa). Across these conditions, the phase-specific structural trends remain consistent: γ-Fe_2O_3 develops porosity, while Fe_3O_4 remains structurally compact (Figures S2–S4 and S6–S9, Supporting Information). This consistency across pressure regimes suggests that the observed differences are governed primarily by intrinsic defect chemistry of oxides—namely, the presence or absence of intrinsic Fe vacancies—rather than by external pressure. While higher pressure can influence reaction kinetics, the dominant reduction pathways and defect evolution are determined by lattice thermodynamics and defect stability. These results support the extrapolation of our atomic-scale insights to more industrially relevant conditions and highlight the critical role of defect chemistry in H_2-based ironmaking.

Beyond steelmaking, these insights have broader relevance for catalysis. Nanoscale Fe oxides are widely used in

heterogeneous catalysis,[55–57] and the contrasting vacancy behaviors of γ-Fe_2O_3 and Fe_3O_4 offer complementary advantages. In γ-Fe_2O_3, vacancy clustering induces intrinsic nanoporous architectures, which increase surface area, expose a high density of active sites, and enhance mass transport—key attributes for catalytic applications like gas-phase oxidation or photocatalysis.[58,59] Conversely, the resistance to vacancy clustering in Fe_3O_4 preserves structural integrity, making it well-suited for applications demanding mechanical stability and long-term durability under harsh conditions, such as high-temperature catalysis or electrochemical water splitting.[60–62] By integrating these oxides into hybrid catalytic systems, it is possible to leverage γ-Fe_2O_3's high reactivity alongside Fe_3O_4's durability. Such designs enable synergistic performance gains, where porous γ-Fe_2O_3 domains act as reactive hotspots while Fe_3O_4 scaffolds ensure long-term stability. Furthermore, vacancy engineering offers a powerful lever to tailor electronic properties: γ-Fe_2O_3's defect-rich interfaces can modulate charge transfer and adsorbate binding, while the ordered lattice in Fe_3O_4 ensures consistent electronic environments, enabling stable and selective catalysis. Together, these results highlight the potential of vacancy dynamics to dictate both functional performance and process efficiency. From hydrogen metallurgy to energy conversion and environmental remediation, tailoring defect structures in iron oxides opens paths toward next-generation catalytic materials that balance high activity with operational resilience.

4. Conclusion

This study elucidates the atomic-scale mechanisms governing the hydrogen-driven reduction of γ-Fe_2O_3 to Fe_3O_4, revealing the critical role of vacancy dynamics in shaping structural evolution and reaction kinetics. A key finding is the stark contrast in defect behavior between the two oxides: in γ-Fe_2O_3, O vacancies preferentially aggregate around intrinsic Fe vacancies, forming a porous structure. In contrast, Fe_3O_4 remains dense and pore-free due to its high O vacancy formation energy and the absence of stabilizing Fe vacancies, effectively suppressing defect clustering. This divergence in defect dynamics directly influences the phase transformation pathway. In γ-Fe_2O_3, vacancy clustering locally depletes lattice O deficiency, thereby impeding Fe_3O_4 nucleation within the γ-Fe_2O_3 bulk. As a result, phase transformation is confined to the γ-Fe_2O_3/Fe_3O_4 interface, where it proceeds via linear displacement—indicative of interface-reaction-limited kinetics. In contrast, Fe_3O_4, with its more uniformly distributed vacancies, supports a steady increase in lattice O deficiency, enabling progressive nucleation of lower oxides such as FeO. More broadly, the contrasting porosity behaviors of γ-Fe_2O_3 (nanoporous) and Fe_3O_4 (dense) highlight the fundamental importance of vacancy dynamics in determining both process efficiency and functional performance. In hydrogen metallurgy, controlling vacancy aggregation can mitigate pore formation and accelerate reduction rates. In catalyst design, tailoring vacancy distribution offers a powerful strategy to optimize the balance of activity, selectivity, and structural durability. Together, these insights highlight vacancy engineering as a versatile tool for advancing both energy-efficient steelmaking and high-performance oxide-based catalytic systems.

5. Experimental Section

Material Preparation: The α-Fe_2O_3 samples used for the reduction experiments were prepared through thermal oxidation of polycrystalline Fe foils (99.99% purity). Prior to oxidation, the Fe foils were thoroughly rinsed with deionized water and ultrasonicated in acetone for 5 minutes to remove any residual contaminants. The cleaned foils were placed on a substrate heater inside a vacuum chamber, with the sample temperature closely monitored using a K-type thermocouple in direct contact with the heater.

Oxidation was initiated by evacuating the chamber to a base pressure of $\approx 3 \times 10^{-4}$ Pa. High-purity O_2 gas (99.999%) was then introduced until the chamber pressure reached 270 Pa, after which the chamber was sealed. The Fe samples were heated at a rate of $\approx$20 °C min^{-1} to 600 °C and held isothermally for 60 min in the O_2 atmosphere. This oxidation process resulted in the formation of well-crystallized α-Fe_2O_3 nanostructures (nanowires and nanoblades) on the Fe substrate.[20–24] The α-Fe_2O_3 layer was scratched off the Fe substrate and dispersed in isopropanol via ultrasonication. The resulting suspension was drop-cast onto silicon nitride (SiNx) membrane TEM grids, which were subsequently loaded onto a heating holder and inserted into the environmental TEM.

In Situ TEM Imaging: In situ monitoring of oxide reduction was carried out using a dedicated environmental TEM equipped with an objective-lens aberration corrector and a gas manifold system, enabling precise control over the gas flow rate and pressure within the specimen area.

During the experiments, high-purity H_2 gas (99.999%) was passed through a liquid N_2 trap to remove moisture by condensing water molecules. H_2 gas was then introduced into the TEM specimen area at $\approx$0.5 Pa. The sample was heated to 500 °C under the H_2 flow, enabling direct observation of the reduction process. A series of in situ characterizations—including HRTEM imaging and video recording, nanobeam electron diffraction, and EELS—was performed under these conditions. HRTEM imaging of the reduction process was recorded at a frame rate of 0.5 s per frame to capture the dynamic structural evolution (Figures 1–4; Figures S2–S4, Supporting Information).

All in situ TEM experiments were conducted using α-Fe_2O_3 nanoblades synthesized via thermal oxidation of Fe foil, followed by H_2 reduction at 500 °C under 0.5 Pa H_2. Figures 1–4 capture different spatial regions and time points within the same experiment or series of experiments under identical sample preparation and reduction conditions. Specifically: Figure 1 provides an overview of the α-Fe_2O_3 → γ-Fe_2O_3 → Fe_3O_4 transformation sequence; Figure 2 focuses on nanocavity formation within γ-Fe_2O_3; Figure 3 highlights interfacial dynamics at the γ-Fe_2O_3/Fe_3O_4 boundary; and Figure 4 captures the later-stage Fe_3O_4-to-FeO transformation within the bulk. Due to rapid kinetics and sample drift following H_2 introduction, the initial α-Fe_2O_3 → γ-Fe_2O_3 transition could not be captured in detail. Imaging becomes feasible only after the sample stabilizes, by which time γ-Fe_2O_3 has already formed. Consequently, our analysis centers on the subsequent, more structurally distinct and mechanistically informative transformations involving γ-Fe_2O_3, Fe_3O_4, and FeO.

EELS analysis was conducted to determine the oxidation state of the reduced oxide. After background removal from the spectra, the data were deconvoluted, and two arctangent functions were applied to subtract the post-edge background. This process isolated the Fe L_3 and L_2 edges, allowing calculation of the L_3/L_2 ratio (white line ratio), which correlates with the oxidation state of Fe. To prevent unintended oxide reduction due to electron beam exposure, the electron beam was blanked between data acquisition sessions. Additionally, the potential effect of electron beam irradiation on reduction behavior was assessed by comparing areas exposed to the beam with unexposed regions. The results confirmed that electron beam irradiation had a negligible effect on the reduction process.[20]

Ex-Situ TEM Characterization: Ex-situ characterization of the reduced samples following the environmental TEM experiments was performed using HAADF-STEM on FEI Talos F200X, with EDS analysis conducted in the same regions (Figures S8c,d and S9, Supporting Information). Additional atomic-scale HAADF imaging was conducted using a probe-corrected STEM (Hitachi 2700) (Figure 5c–h). For comparison, as-prepared α-Fe_2O_3 samples were also directly reduced in a vacuum chamber at 500 °C under

H_2 pressures of ≈270 Pa (Figure S3, Supporting Information) and ≈700 Pa (Figure 5a,b; Figure S7, Supporting Information).

DFT Calculation: DFT calculations were performed using the Vienna Ab initio Simulation Package (VASP)[63–66] with a plane-wave basis set and an energy cutoff of 520 eV for representing valence electron states. Exchange-correlation interactions were treated using the generalized gradient approximation (GGA),[63–66] specifically with the Perdew-Burke-Ernzerhof (PBE) functional.[67] To account for the strong correlation effects associated with the partially filled Fe 3d orbitals, a Hubbard parameter (U) of 3.8 eV.[68] was applied to the Fe 3d states, following the established GGA+U approach based on prior research.

Fe_3O_4 and γ-Fe_2O_3 bulk models were used to investigate vacancy clustering. Brillouin zone sampling was conducted using a (6 × 6 × 6) k-point grid generated within the Monkhorst-Pack scheme.[69] For the γ-Fe_2O_3 bulk model with Fe vacancies, a (6 × 6 × 1) k-point grid was employed. Structural relaxations were carried out using the conjugate gradient method, ensuring convergence of atomic forces below 0.015 eV $Å^{-1}$. The calculated lattice parameter for Fe_3O_4 was 8.456 Å, aligning closely with both previous computational studies and experimental measurements of 8.44 Å.[20,21,49] The γ-Fe_2O_3 bulk model was constructed using three Fe_3O_4 blocks containing eight Fe vacancies to reflect the intrinsic defect structure.[49]

Supporting Information

Supporting Information is available from the Wiley Online Library or from the author.

Acknowledgements

Y.P. Wu and D.X. Wu contributed equally to this work. This work was supported by the U.S. National Science Foundation under Grant No. DMR-2303712. S. Ye acknowledges support from the U.S. Department of Energy (DOE), Office of Basic Energy Sciences, Division of Materials Sciences and Engineering, under Award No. DE-SC0001135. This research utilized the electron microscopy and theory/computation resources at the Center for Functional Nanomaterials, a U.S. DOE Office of Science User Facility at Brookhaven National Laboratory, under Contract No. DE-SC0012704. Additional computational support was provided by the Spiedie cluster at the State University of New York at Binghamton.

Conflict of Interest

The authors declare no conflict of interest.

Data Availability Statement

The data that support the findings of this study are available in the supplementary material of this article.

Keywords

hydrogen direction reduction of iron ore, in situ environmental transmission electron microscopy, phase transformations, vacancy

Received: July 26, 2025
Revised: September 27, 2025
Published online:

[1] A. Eliyahu-Behar, N. Yahalom-Mack, Y. Gadot, I. Finkelstein, *J. Archaeol. Sci.* **2013**, *40*, 4319.
[2] J. Ogbezode, O. Ajide, O. Ofi, O. Oluwole, *Res. Dev. Mater. Sci.* **2022**, *17*, 1992.
[3] C. Lan, Q. Sun, J. Shao, S. Zhang, R. Liu, J. Lu, H. Liu, Q. Lyu, *Int. J. Hydrog. Energy* **2024**, *86*, 465.
[4] T. A. Rickard, *Am. J. Archaeol.* **1939**, *43*, 85.
[5] H. Springer, I. R. Souza Filho, L. Choisez, M. A. Zarl, C. Quick, A. Horn, J. Schenk, *Sustain. Mater. Technol.* **2024**, *39*, 00785.
[6] D. Raabe, *Chem. Rev.* **2023**, *123*, 2436.
[7] T. Ariyama, K. Takahashi, Y. Kawashiri, T. Nouchi, *J. Sustain. Metall.* **2019**, *5*, 276.
[8] P. M. Falcone, M. Hiete, A. Sapio, *Curr. Opin. Green Sustain. Chem.* **2021**, *31*, 100506.
[9] V. Vogl, M. Åhman, L. J. Nilsson, *J. Clean. Prod.* **2018**, *203*, 736.
[10] N. Gallegos, M. Apecetche, *J. Mater. Sci.* **1988**, *23*, 451.
[11] Y. Ma, I. R. Souza Filho, X. Zhang, S. Nandy, P. Barriobero-Vila, G. Requena, D. Vogel, M. Rohwerder, D. Ponge, H. Springer, *Int. J. Miner. Metall. Mater.* **2022**, *29*, 1901.
[12] Y. Ma, J. W. Bae, S. H. Kim, M. Jovičević-Klug, K. Li, D. Vogel, D. Ponge, M. Rohwerder, B. Gault, D. Raabe, *Adv. Sci.* **2023**, *10*, 2300111.
[13] M. Pei, M. Petäjäniemi, A. Regnell, O. Wijk, *Metals* **2020**, *10*, 972.
[14] L. Braun, J. Spielmann, D. E. Doronkin, C. Kuhn, A. Maliugin, D. I. Sharapa, I. Huck, J. Bao, S. Tischer, F. Studt, O. Deutschmann, U. I. Kramm, J.-D. Grunwaldt, *ChemSusChem* **2024**, *17*, 202401045.
[15] H.-Y. Lin, Y.-W. Chen, C. Li, *Thermochim. Acta* **2003**, *400*, 61.
[16] J. Zieliński, I. Zglinicka, L. Znak, Z. Kaszkur, *Appl. Catal. A: Gen.* **2010**, *381*, 191.
[17] X. Zheng, S. Paul, L. Moghimi, Y. Wang, R. A. Vilá, F. Zhang, X. Gao, J. Deng, Y. Jiang, X. Xiao, *Proc. Natl. Acad. Sci. USA* **2023**, *120*, 2305097120.
[18] Z. Zhou, Y. Wu, W. Zhu, L. Qiao, S. Ye, X. Chen, M. Li, D. Zakharov, R. Sharma, J. Yang, G. Zhou, *ACS Appl. Mater. Interfaces* **2025**, *17*, 42380.
[19] D. Spreitzer, J. Schenk, *Steel Res. Int.* **2019**, *90*, 1900108.
[20] W. Zhu, J. P. Winterstein, W.-C. D. Yang, L. Yuan, R. Sharma, G. Zhou, *ACS Nano* **2017**, *11*, 656.
[21] W. Zhu, J. Winterstein, I. Maimon, Q. Yin, L. Yuan, A. N. Kolmogorov, R. Sharma, G. Zhou, *J. Phys. Chem. C* **2016**, *120*, 14854.
[22] X. Liu, Y. Pan, J. Zhao, Y. Wang, M. Ge, L. Qian, L. Zhang, L. Gu, D. Zhou, D. Su, *J. Am. Chem. Soc.* **2024**, *146*, 17487.
[23] L. Yuan, Q. Jiang, J. Wang, G. Zhou, *J. Mater. Res.* **2012**, *27*, 1014.
[24] L. Yuan, Y. Wang, R. Cai, Q. Jiang, J. Wang, B. Li, A. Sharma, G. Zhou, *Mater. Sci. Eng. B* **2012**, *177*, 327.
[25] A. Aharoni, E. H. Frei, M. Schieber, *J. Phys. Chem. Solids* **1962**, *23*, 545.
[26] K. Jenkinson, M. C. Spadaro, V. Golovanova, T. Andreu, J. R. Morante, J. Arbiol, S. Bals, *Adv. Mater.* **2023**, *35*, 2306447.
[27] J. Dai, Y. Sun, Z. Liu, Y. Zhang, S. Duan, R. Wang, *Angew. Chem.* **2024**, *136*, 202409673.
[28] H.-Y. Chao, K. Venkatraman, S. Moniri, Y. Jiang, X. Tang, S. Dai, W. Gao, J. Miao, M. Chi, *Chem. Rev.* **2023**, *123*, 8347.
[29] L. Zou, P. Cao, Y. Lei, D. Zakharov, X. Sun, S. D. House, L. Luo, J. Li, Y. Yang, Q. Yin, *Nat. Commun.* **2020**, *11*, 3934.
[30] R. Sainju, T. Li, M. R. Nielsen, Y. Zhu, *Nano Lett.* **2025**, *25*, 10521.
[31] A. Yoon, L. Bai, F. Yang, F. Franco, C. Zhan, M. Rüscher, J. Timoshenko, C. Pratsch, S. Werner, H. S. Jeon, M. C. D. O. Monteiro, S. W. Chee, B. Roldan Cuenya, *Nat. Mater.* **2025**, *24*, 762.
[32] L. Yuan, R. Cai, J. Jang, W. Zhu, C. Wang, Y. Wang, G. Zhou, *Nanoscale* **2013**, *5*, 7581.
[33] T. Li, H. Feng, Y. Wang, C. Wang, W. Zhu, L. Yuan, G. Zhou, *J. Cryst. Growth* **2018**, *498*, 10.
[34] M. Kakran, N. G. Sahoo, I.-L. Tan, L. Li, *J. Nanoparticle Res.* **2012**, *14*, 757.
[35] A. M. Glezer, V. Stolyarov, A. A. Tomchuk, N. A. Shurygina, *Tech. Phys. Lett.* **2016**, *42*, 51.
[36] W. Bollmann, *Crystal defects and crystalline interfaces*, Springer-Verlag Berlin Heidelberg, Berlin & Heidelberg **2012**.

[37] R. C. Baetzold, H. Yang, *J. Phys. Chem. B* **2003**, *107*, 14357.
[38] X. Yu, C.-F. Huo, Y.-W. Li, J. Wang, H. Jiao, *Surf. Sci.* **2012**, *606*, 872.
[39] C. Fan, R. G. S. Annadanam, Z. Shang, J. Li, M. Li, H. Wang, A. El-Azab, X. Zhang, *Acta Mater.* **2020**, *201*, 504.
[40] W. B. Liu, N. Wang, Y. Z. Ji, P. C. Song, C. Zhang, Z. G. Yang, L. Q. Chen, *J. Nucl. Mater.* **2016**, *479*, 316.
[41] X. Huang, T. Jones, H. Fan, M.-G. Willinger, *Nanoscale* **2017**, *9*, 12479.
[42] G. M. Han, H. Wang, D.-Y. Lin, X. Y. Zhu, S. Y. Hu, H. F. Song, *Comput. Mater. Sci.* **2017**, *133*, 22.
[43] S. B. Simonsen, I. Chorkendorff, S. Dahl, M. Skoglundh, J. Sehested, S. Helveg, *J. Catal.* **2011**, *281*, 147.
[44] A. K. Datye, Q. Xu, K. C. Kharas, J. M. McCarty, *Catal. Today* **2006**, *111*, 59.
[45] X. Chen, C. Li, B. Li, Y. Ying, S. Ye, D. N. Zakharov, S. Hwang, J. Fang, G. Wang, Y.-J. Hu, *ACS Nano* **2024**, *18*, 31160.
[46] E. Terrier, Y. Liu, S. Begin, B. Pichon, J. Bigot, V. Halte, *Acta Phys. Pol. A* **2015**, *127*, 345.
[47] X. Chen, J. Wang, S. B. Patel, S. Ye, Y. Wu, Z. Zhou, L. Qiao, Y. Wang, N. Marinkovic, M. Li, S. Hwang, D. N. Zakharov, L. Ma, Q. Wu, J. A. Boscoboinik, J. C. Yang, G. Zhou, *Nature* **2025**, *644*, 927.
[48] X. Sun, D. Wu, L. Zou, S. D. House, X. Chen, M. Li, D. N. Zakharov, J. C. Yang, G. Zhou, *Nature* **2022**, *607*, 708.
[49] R. Grau-Crespo, A. Y. Al-Baitai, I. Saadoune, N. H. De Leeuw, *J. Phys. Condens. Matter* **2010**, *22*, 255401.
[50] D. H. Lindsley, *Oxide Minerals: Petrologic and Magnetic Significance*, De Gruyter, Berlin & Boston **2018**.
[51] G. Van Oosterhout, C. Rooijmans, *Nature* **1958**, *181*, 44.
[52] H. Furukawa, F. Gándara, Y.-B. Zhang, J. Jiang, W. L. Queen, M. R. Hudson, O. M. Yaghi, *J. Am. Chem. Soc.* **2014**, *136*, 4369.
[53] F. R. Leivas, M. Zhao, A. Allemand, C. Cottin-Bizonne, S. M. M. Ramos, M. C. Barbosa, A.-L. Biance, *Langmuir* **2025**, *41*, 15578.
[54] C. Huan, P. Wang, B. He, Y. Cai, Q. Ke, *J. Mater. Chem. C* **2022**, *10*, 1839.
[55] H. Feng, Y. Wang, C. Wang, F. Diao, W. Zhu, P. Mu, L. Yuan, G. Zhou, F. Rosei, *Nanotechnology* **2016**, *27*, 295703.
[56] H. Fu, Q. Chen, B. Min, S. Li, X. Chen, L. Ling, *Fundam. Res.* **2024**, https://doi.org/10.1016/j.fmre.2023.10.023.
[57] A. L.-T. Pham, C. Lee, F. M. Doyle, D. L. Sedlak, *Environ. Sci. Technol.* **2009**, *43*, 8930.
[58] B. Rungtaweevoranit, A. M. Abdel-Mageed, P. Khemthong, S. Eaimsumang, K. Chakarawet, T. Butburee, B. Kunkel, S. Wohlrab, K. Chainok, J. Phanthasri, *ACS Appl. Mater. Interfaces* **2023**, *15*, 26700.
[59] C. Yang, P. Wang, J. Li, Q. Wang, P. Xu, S. You, Q. Zheng, G. Zhang, *Chem. Eng. J.* **2021**, *417*, 129340.
[60] M. Liu, Y. Ye, J. Ye, T. Gao, D. Wang, G. Chen, Z. Song, *Magnetochemistry* **2023**, *9*, 110.
[61] B. Qian, X. Wang, J. Xu, H. Liu, H. Zhou, H. Li, X. Wen, C. Liu, Y. Hu, Q. Guo, *Sustain. Mater. Technol.* **2025**, *43*, 01330.
[62] S. Li, L. Huang, Q. Zhang, H. Lin, R. Wang, C. Feng, Y. Xu, Y. Jiao, L. You, J. Chen, *Int. J. Hydrog. Energy* **2024**, *49*, 103.
[63] G. Kresse, J. Furthmüller, *Phys. Rev. B* **1996**, *54*, 11169.
[64] G. Kresse, J. Furthmüller, *Comput. Mater. Sci.* **1996**, *6*, 15.
[65] G. Kresse, D. Joubert, *Phys. Rev. B* **1999**, *59*, 1758.
[66] P. E. Blöchl, *Phys. Rev. B* **1994**, *50*, 17953.
[67] J. P. Perdew, K. Burke, M. Ernzerhof, *Phys. Rev. Lett.* **1996**, *77*, 3865.
[68] Z. Fu, B. Yang, Y. Zhang, N. Zhang, Z. Yang, *J. Catal.* **2018**, *364*, 291.
[69] H. J. Monkhorst, J. D. Pack, *Phys. Rev. B* **1976**, *13*, 5188.